Heterogeneously Integrated AlGaAs/GaAs Photodiodes on Tantala Waveguides

Masoud Jafari, *Graduate Student Member, IEEE*, Tasneem Fatema, *Graduate Student Member, IEEE*, David R. Carlson, Scott B. Papp, and Andreas Beling, *Senior Member, IEEE*

***Abstract*—We demonstrate the first heterogeneously integrated high-speed waveguide photodiode on tantalum pentoxide (Ta_2O_5, or tantala) for visible light detection. The PDs have 100 pA dark current, more than 56% quantum efficiency (QE) between 635 nm and 780 nm wavelengths, and up to 16 GHz bandwidth. We also measured open eye diagrams at 12 Gbit/s - the upper limit of our experimental setup.**

***Index Terms*—GaAs photodetector, tantala waveguide, heterogeneous integration.**

I. Introduction

Waveguide-based integrated photonics utilizing tantala has garnered significant attention owing to the material's favorable nonlinear and mechanical characteristics. Due to its large bandgap, tantala is transparent across a wide spectral range, extending from 320 nm well into the infrared region, and tantala waveguides with low loss have been demonstrated [1]. Tantala possesses a real refractive index slightly above 2 and a Kerr index that is approximately three times higher than silicon nitride (Si_3N_4) [2]. Together with its low thermo-optic coefficient, tantala is well-suited for integrated nonlinear photonics applications including supercontinuum generation and soliton frequency comb generation spanning from the visible to the far-infrared wavelengths. Recently, the use of an optical cavity in tantala integrated with an InGaAs quantum-well on top has also resulted in a first demonstration of a heterogeneously integrated laser on this platform [3].

To further enhance the functionality of the tantala platform, we report in this paper on the first high-speed heterogeneously integrated AlGaAs/GaAs photodiode (PD) on tantala. Heterogeneous integration of group III-V materials on non-native photonic platforms has been demonstrated as a technique to integrate dissimilar materials without compromising their own properties [4], [5]. Among the available integration techniques, adhesive die-to-wafer bonding is a versatile low-temperature backend process based on epoxy-based photoresist which can tolerate a considerable amount of surface roughness [6], [7]. In contrast to micro-transfer printing which relies on device-level pick-and-place [8], die-to-wafer bonding has lithography-defined alignment precision. Similar to heteroepitaxial [9] and monolithic growth, the approach is scalable and wafer throughput can be high. Moreover, it provides additional flexibility in device integration since it is free from constraints posed by lattice mismatch of the different material systems [10]. Distinct from waveguide silicon PDs that have been previously employed for on-chip visible light detection [11] [12], GaAs-based heterostructure PDs can offer advantages, including high carrier drift velocities, electron velocity overshoot, and a direct bandgap, potentially resulting in higher bandwidth and stronger absorption. Importantly, GaAs and its lattice-matched compounds like AlGaAs offer cut-off wavelengths ranging from 872 nm to below 646 nm, depending on their compositions. This property makes bandgap engineering available, and thus allows for a composition of highly absorbing and transparent layers. It should be mentioned that GaAs-based material has been frequently used in PIN and Schottky photodetectors for applications around 850 nm wavelength and has produced photodetectors on native substrate with high efficiencies, large bandwidths, and low dark currents [13], [14], [15]. In the following, we describe design, fabrication, and characterization of high-speed PDs that can find applications in tantala photonic integrated circuits at wavelengths 600–850 nm. While we use 150 nm-thick waveguides in this work, we expect that our approach can also be applied to thicker waveguides (e.g. 600 nm), as recently demonstrated for thin film lithium niobate (TFLN) at 1550 nm [7].

II. Design

Fig. 1 presents a schematic view of the integrated PD. Light is evanescently coupled from the tantala trench waveguide into the 600-nm thick intrinsic GaAs absorber, which is embedded between layers with wider bandgaps [16]. Due to their lower refractive indices, these layers function as optical claddings, and help confining the light within the absorber. To reduce absorption in the highly doped contact layers, we used $Al_{0.4}Ga_{0.6}As$ with a bandgap wavelength of 646 nm. Reducing carrier generation in these layers at the operational wavelength is crucial to minimize

Manuscript received 19 March 2024; revised 31 May 2024 and 30 June 2024; accepted 7 July 2024. Date of publication 10 July 2024; date of current version 2 December 2024. This work was supported by the Defense Advanced Research Projects Agency (DARPA) through the LUMOS Program, under Contract HR0011-20-2-0046. *(Corresponding author: Masoud Jafari.)*

Masoud Jafari, Tasneem Fatema, and Andreas Beling are with the Department of Electrical and Computer Engineering, University of Virginia, Charlottesville, VA 22904 USA (e-mail: mj2mf@virginia.edu).

David R. Carlson is with Octave Photonics, Louisville, CO 80027 USA.

Scott B. Papp is with the Time and Frequency Division, National Institute of Standards and Technology, Boulder, CO 80305 USA.

Color versions of one or more figures in this article are available at https://doi.org/10.1109/JLT.2024.3425793.

Digital Object Identifier 10.1109/JLT.2024.3425793

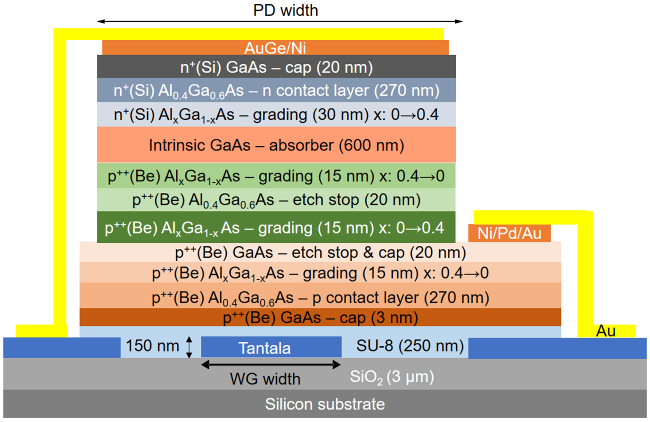

Fig. 1. PD layer stack on tantala waveguide.

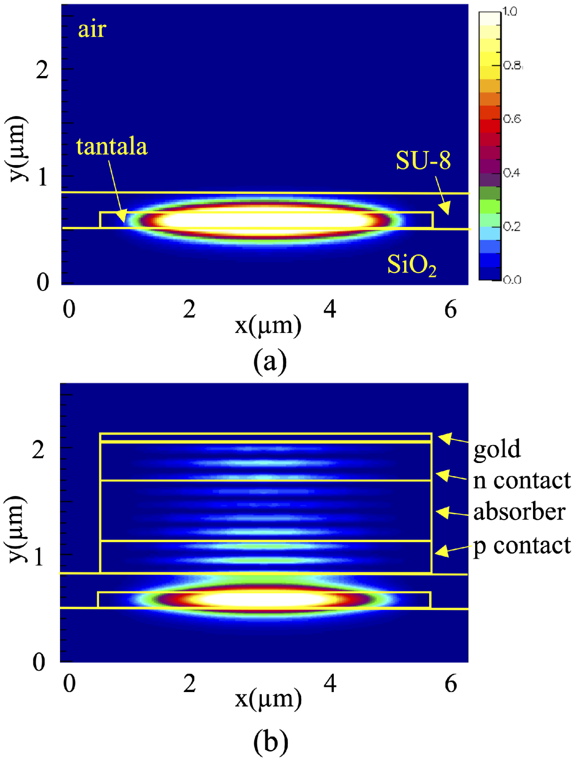

Fig. 2. Simulated optical intensity at 780 nm in (a) tantala waveguide, and (b), heterogeneous PD (after 5 μm in direction of light propagation). The simulated coupling efficiency from the fundamental mode in the tantala waveguide into guided modes in the PD region was close to 100%, and reflections were negligible.

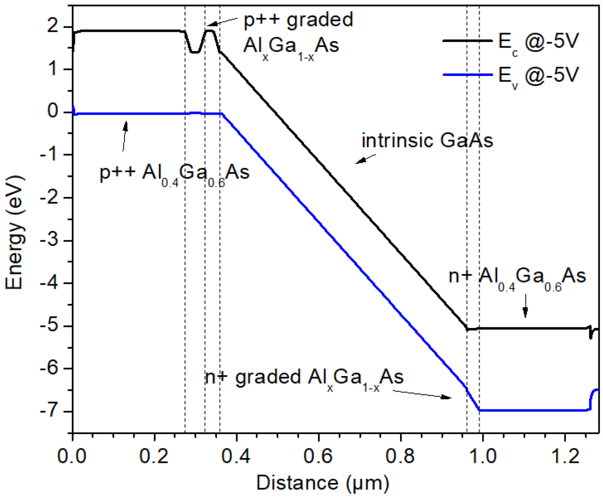

Fig. 3. Simulated energy band diagram.

potential slow carrier diffusion or recombination. We chose SU-8 as the bonding agent, since it is transparent in the visible spectral range and can be used for surface planarization. The SU-8 thickness was designed to be 250 nm, resulting in 423 nm distance between the tantala waveguide and the absorber, for a high optical coupling efficiency. Using commercial software (Fimmwave by Photon Design), Figs. 2(a) and (b) show simulations of the optical intensity distribution in the cross sections of the tantala waveguide and the PD, respectively. Based on our simulations, we did not expect significant changes in optical coupling efficiency for variations in SU-8 thickness of ± 50 nm. To enhance carrier transport, bandgap-graded $Al_xGa_{1-x}As$ layers are carefully designed to minimize band offsets at the interfaces. Fig. 3 shows the energy band diagram. Etch stop and cap layers are introduced to facilitate the fabrication process and prevent oxidation. The rectangular PD double mesa structures are integrated atop waveguides and connected to 50 Ω coplanar waveguide (CPW) radio frequency (RF) probe pads through airbridges for high-frequency testing. The 150 nm-thick tantala waveguide with a constant width (WG width) of 5 μm underneath the PD is un-cladded on the top and has SiO_2 as the lower cladding.

III. FABRICATION

The PD epitaxial layer stack was grown lattice-matched on GaAs substrate by molecular beam epitaxy. Using a thin layer (250 nm) of SU-8 we bonded a ca. 50 mm^2 wafer die onto the tantala chip that was pre-fabricated with waveguides utilizing ion-beam sputtering (Fig. 4(a) and (b)). The GaAs substrate removal involved nitric acid, followed by citric acid, and a potassium iodine (KI) dilution to selectively etch the AlGaAs etch stop layer. This etching sequence has advantages over alternative high aluminum content AlGaAs etchants, such as hydrofluoric acid, as it helps preserve the SiO_2 cladding layer at the waveguide facets, and thus eliminating the need for additional post-processing steps. The n- and p-mesa were patterned using direct laser writing, and we used wet etching including KI dilution and citric acid to selectively etch the AlGaAs and GaAs layers, respectively. Fig. 4(c) shows the PD after double mesa formation on the tantala waveguide. Metal contacts were deposited through electron beam evaporation, followed by lift-off. To achieve low contact resistance, we used a stack of Ni (80 nm), Pd (120 nm), and Au (200 nm), for the p-contact metal, which becomes ohmic with a specific contact resistivity of $7.6\times10^{-4}\Omega$ cm^2 after a 5-minute annealing process in an N_2 environment at 300 °C. The n-contact metal comprises AuGe (200 nm) and

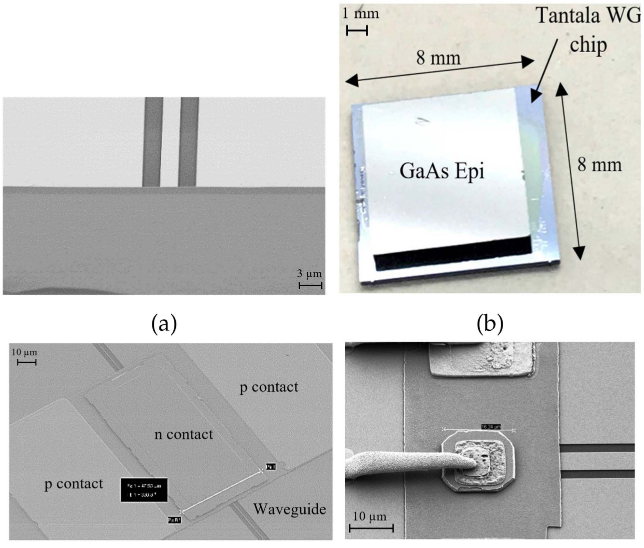

(a) (b)

(c) (d)

Fig. 4. (a) Tantala waveguide at the chip facet, (b) GaAs epitaxial layers bonded onto tantala waveguide (WG) chip before substrate removal, (c) PD after mesa etching, and (d) PD with airbridge connecting to probe pad.

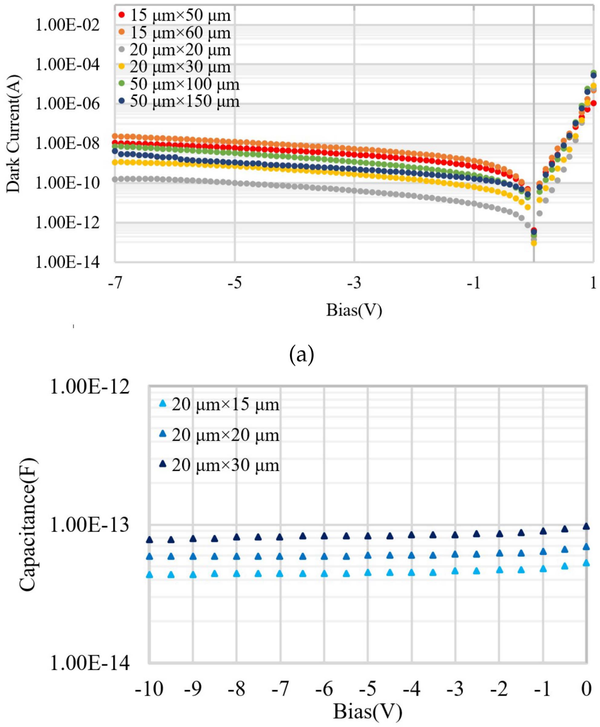

(a)

(b)

Fig. 5. Dark current (a) and (b) capacitance measurements at 1 MHz of PDs with different areas.

Ni (56 nm), exhibiting ohmic behavior with a specific contact resistivity of $5.3\times10^{-4}\Omega\text{cm}^2$ after a 1-minute annealing process in an N_2 environment at 350 °C, as determined from transfer length method measurements. It should be mentioned that we did not observe any impact from the annealing on the adhesive bonding layer which aligns with reports on thermal stability of SU-8 in [17]. Finally, CPW RF probe pads were incorporated and connected to the p- and n-mesa through Au-plated air bridges (Fig. 4(d)). Based on our experience, it was safe to use n-methyl-2-pyrrolidone (NMP) at 70 °C for several minutes in an ultrasonic bath for lift-off, and we noticed no degradation of the bond.

IV. EXPERIMENTAL RESULTS

Fig. 5(a) depicts the measured dark currents of the fabricated PDs. Remarkably low dark currents, reaching 100 pA at −7 V, were measured for PDs with a small active area of $20 \times 20\ \mu\text{m}^2$ (PD width × PD length). Typical dark current densities at −5 V were well below 1 mA/cm^2, with one PD as low as 15 μA/cm^2. While this is higher than the dark current density reported for transfer-printed GaAs PDs on silicon nitride waveguides [18] and GaAs PDs on native substrate [14], it is an order of magnitude lower than that of heterogeneous InGaAs/InP PDs for 1550 nm detection [7] due to the larger bandgap of GaAs. The fact that dark current did not strictly scale with area in our PDs can be attributed to surface leakage, which can be addressed by an appropriate passivation layer [19]. To assess the resistance-capacitance (RC)-limited bandwidth, the PD capacitance was determined using an LCR meter. As illustrated in Fig. 5(b), a PD with $20 \times 15\ \mu\text{m}^2$ nominal area approaches full depletion at −5 V, exhibiting a junction capacitance of 45 fF. This is is 20% lower than calculated from the parallel-plate capacitor model, which can be explained by an area reduction due to some underetch during mesa fabrication. From 0 V to −10 V, the capacitance changes by less than 20% which indicates a low background doping concentration in the intrinsic layer. Factoring in the total series resistance that includes contact resistance (38 Ω) and lateral resistance in the p-contact layer (89 Ω), we estimated an RC-limited bandwidth of 20 GHz with a 50 Ω external load. Responsivity was measured from different PDs at three wavelengths (520 nm, 635 nm, 780 nm) using lensed fibers to couple light from the laser sources into the tantala waveguides. To determine the internal responsivity (and internal QE), we measured the photocurrent and input optical power. The latter was accounted for the fiber-to-chip coupling losses of 4.5 dB, 7 dB and 8.5 dB at 780 nm, 635 nm, and 520 nm, respectively. Fig. 6 illustrates the dependency of internal responsivity on the PD length at 635 nm wavelength. As the PD length increases, so does the responsivity, and a 150 μm-long device reaches 0.3 A/W corresponding to 58% QE. As shown in Fig. 7, a similar QE is measured at 780 nm, and no significant dependence on PD bias was observed. The simulated QE for this PD was 66%. Our simulation suggests that absorption in the top metal contact and in the highly doped GaAs etch stop and cap layers are the limiting factors in the current design. Therefore, further increasing the PD length will not significantly improve QE. We expect that a higher QE can be achieved in future designs by decreasing the thickness of the GaAs etch stop layer and moderately increasing the absorber thickness. It should be mentioned that QE at 520 nm was lower, which we attribute to strong photon absorption in the

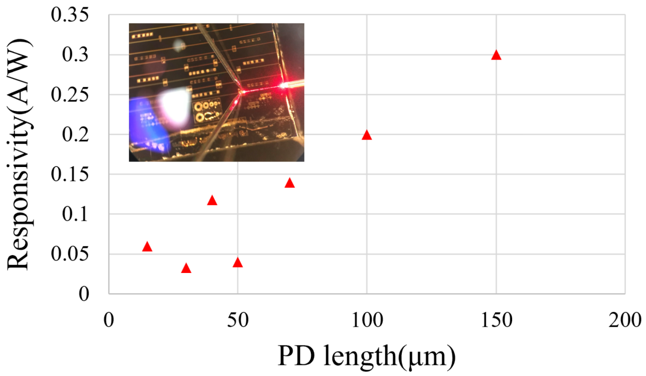

Fig. 6. Internal responsivity vs. PD length at 635 nm wavelength and −5 V. Inset: on-chip testing.

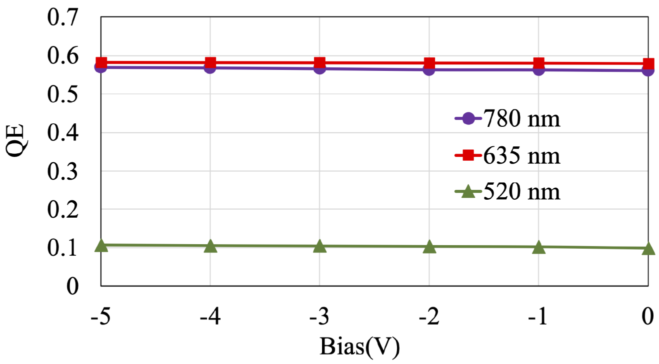

Fig. 7. Internal QE of 50 × 150 μm^2 PD.

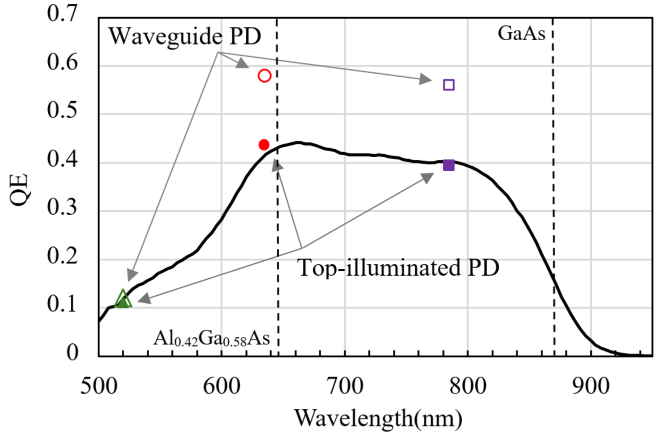

Fig. 8. Measured (line), and calculated (closed symbols) QE of top-illuminated PD. Open symbols represent QE of waveguide PD. Dashed lines: Bandgap wavelengths of $Al_{0.42}Ga_{0.58}As$ and GaAs.

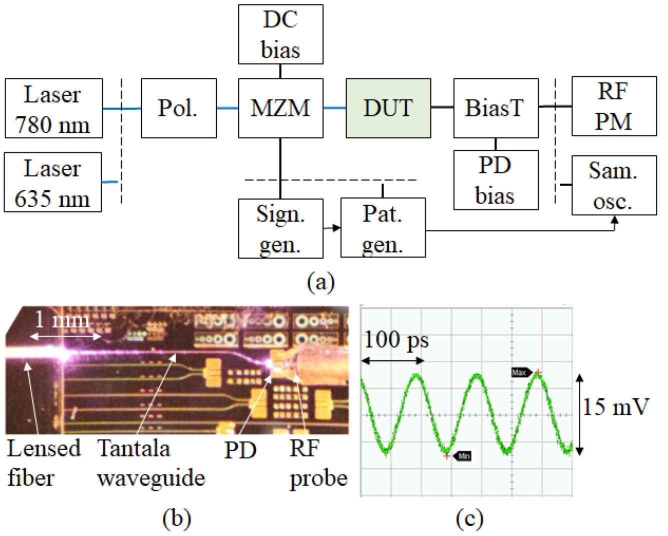

Fig. 9. (a) High-frequency measurement setup. Pol: polarization controller, Sign. gen: RF signal generator, Pat. gen.: pattern generator, DUT: device unnder test, RF PM: RF powermeter, Sam. osc.: sampling oscilloscope. (b) On-chip high-frequency testing. (c) Detected RF waveform at 10 GHz with signal generator power of 12 dBm and 0.5 mA average photocurrent.

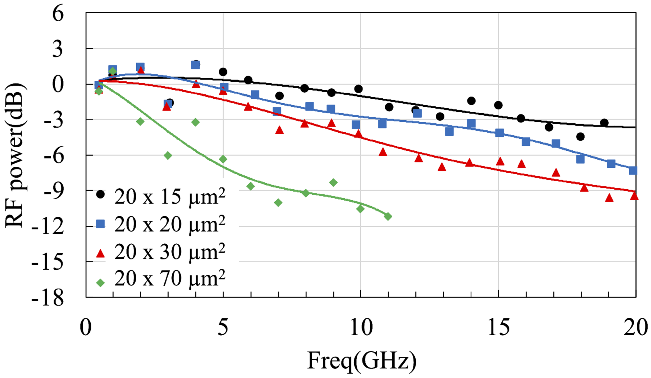

Fig. 10. Frequency responses for PDs with different areas. PD bias, average photocurrent, and wavelength were −5 V, 200 μA, and 780 nm, respectively.

highly-doped AlGaAs contact layers that did not contribute to the photocurrent due to carrier recombination.

To verify the spectral range of our PDs we also measured QE of top illuminated PDs on the same chip using a broadband light source followed by a monochromator. Fig. 8 shows QE >40% from 630 nm to 800 nm which is mainly limited by the bandgaps of the AlGaAs contact layers (646 nm) and the GaAs absorber (872 nm). Calculations using absorption coefficients given in [20] confirmed our measurement. Notably, QE of waveguide PDs can be higher than that of top-illuminated PDs which is due to their longer absorption path and an efficient coupling from the waveguide into the PD. It is worth mentioning that in order to increase QE below 640 nm wavelength, contact layers with larger bandgap such as $Al_{0.5}In_{0.5}P$ can be used in future designs.

The PDs' high-frequency characteristics were measured with the setup illustrated in Figs. 9(a) and (b). A Mach-Zehnder modulator (MZM) biased at quadrature with 20 GHz electro-optical bandwidth (Ixblue MX800nm-LN-20) according to the manufacturer's data sheet was used. To measure the PD's frequency response the MZM was driven with a signal generator. We determined the modulation depth to be 60% at 10 GHz (Fig. 9(c)).

Fig. 10 shows the normalized frequency responses of PDs with different areas measured at 780 nm. In the measurements we used a calibrated RF power meter and subtracted the loss of the

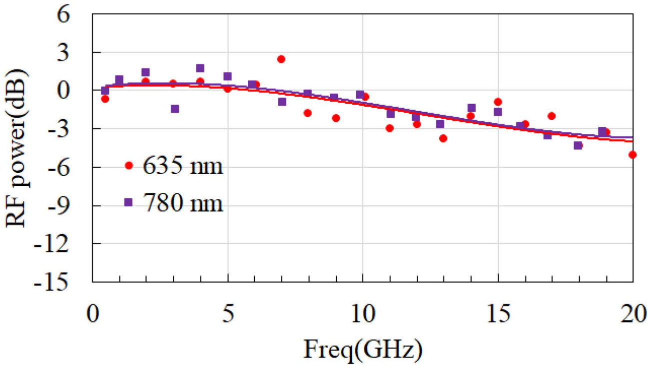

Fig. 11. Frequency responses of 300 μm^2 PD at 635 nm and 780 nm wavelength. The PD bias and average photocurrent were −5 V and 200 μA, respectively.

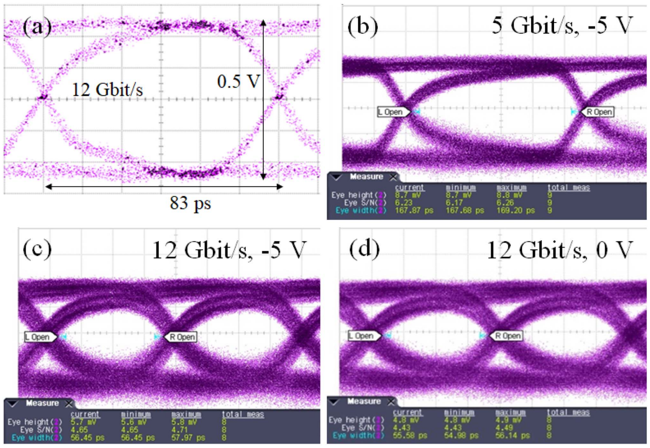

```
                current     minimum     maximum     total meas
Eye height(2)   8.7 mV      8.7 mV      8.8 mV      9
   Eye S/N(2)   6.23        6.17        6.26        9
 Eye width(2)   167.87 ps   167.68 ps   169.20 ps   9
```

```
                current     minimum     maximum     total meas
Eye height(2)   5.7 mV      5.6 mV      5.8 mV      8
   Eye S/N(2)   4.65        4.65        4.71        8
 Eye width(2)   56.45 ps    56.45 ps    57.97 ps    8
```

```
                current     minimum     maximum     total meas
Eye height(2)   4.8 mV      4.8 mV      4.9 mV      8
   Eye S/N(2)   4.43        4.43        4.49        8
 Eye width(2)   55.58 ps    54.98 ps    56.14 ps    8
```

Fig. 12. (a) Electrical eye diagram from pattern generator at 12 Gbit/s. Detected eye diagrams from PD at 0.5 mA average photocurrent: (b) 5 Gbit/s, 5 mV/div, 35 ps/div, PD bias: −5 V, (c), 12 Gbit/s, 5 mV/div, 20 ps/div, PD bias: −5 V, (d) 12 Gbit/s, 5 mV/div, 20 ps/div, PD bias: 0 V.

bias-T and RF cables in the setup from the measured responses. We also corrected for the frequency response of the modulator. As the device area gets smaller, the bandwidth increases which indicates that the PDs are RC-limited. In reasonable agreement with our expectation, we find that a 300 μm^2 PD has a 3 dB bandwidth of 16 GHz, while 600 μm^2 and 1400 μm^2 PDs have 3 dB bandwidths of 8 GHz and 2.5 GHz, respectively. It is worth noting that we also estimated the transit time limited bandwidth using 0.9×10^7 cm/s [21] as the carrier drift saturation velocity in GaAs and obtained >80 GHz, confirming that carrier transit time effects are negligible in our design. Figure 11 compares normalized frequency responses of the same PD measured at 635 nm and 780 nm wavelengths and confirms 16 GHz bandwidth for both wavelengths with a QE of 11%. We expect that bandwidths up to 35 GHz become possible by scaling down the PD width to 10 μm. We initially chose a much larger PD width to ease the fabrication process and allow for direct mesa probing.

For measuring non-return-to-zero eye diagrams we used a pattern generator (Advantest D3186) and a fast sampling oscilloscope (Fig. 9(a)). The pseudo random bit sequence pattern length was 2^{15}-1, and the laser wavelength was 780 nm. Fig. 12(a) shows the electrical eye diagram from the pattern generator at 12 Gbit/s bitrate which was fed into the MZM. Figs. 12(b)–(d) show the eye diagrams of a 20 × 15 μm^2 PD. Clearly open eye diagrams are detected with signal-to-noise ratios of 4.4 and larger. The highest measured bitrate was only limited by our experimental setup, and we expect that our PDs are capable of detecting bitrates beyond 12 Gbit/s. Fig. 12(d) shows a 12 Gbit/s eye diagram of the same device at 0 V showing that detection is largely independent of PD bias.

TABLE I
WAVEGUIDE-INTEGRATED PDS FOR VISIBLE WAVELENGTHS

PD/ waveguide	λ (nm)	QE (%)	gain	BW (GHz)	I_d (nA)	ref.
Si PN[a]/ Si_3N_4	685	40	12	30	0.07	[11]
Si PIN[a]/ Si_3N_4	685	45	9	11	0.003	[22]
Si PN[a]/ Si_3N_4	400–640	60–88	46	9	0.14	[23]
Si PIN[b]/ Si_3N_4	775	30	na	6	0.11	[12]
1400μm^2 GaAs PIN[c]/tantala	635–780	27	na	2.5	1	this work
300μm^2 GaAs PIN[c]/tantala	635–780	11	na	16	0.1	this work

[a]monolithic, [b]micro-transfer printed, [c]wafer-bonded.
BW: bandwidth, I_d: dark current.

V. CONCLUSION

In summary, our integrated PD on tantala waveguide demonstrates 100 pA dark current, QE of 11%, and a bandwidth of 16 GHz suitable for 12 Gbit/s data detection and beyond. This performance approaches, and in some cases already exceeds, that of high-speed waveguide-integrated Si PDs for visible wavelengths on the mature Si_3N_4/Si platform (Table I). With further optimizations of the PD layer design and a reduction in PD area, we expect that the performance can be further improved. We believe that AlGaAs/GaAs waveguide PDs are promising candidates for high-speed tantala photonic integrated circuit applications, and based on our platform-independent scalable integration approach, we anticipate that similar PD designs can also be applied to other photonic platforms such as Si_3N_4 and TFLN to enable high-speed photodetection in the visible spectrum.

REFERENCES

[1] J. A. Black, R. Streater, K. F. Lamee, D. R. Carlson, S.-P. Yu, and S. B. Papp, "Group-velocity-dispersion engineering of tantala integrated photonics," *Opt. Lett.*, vol. 46, no. 4, pp. 817–820, Feb. 2021. [Online]. Available: https://opg.optica.org/ol/abstract.cfm?URI=ol-46-4-817

[2] H. Jung, S.-P. Yu, D. R. Carlson, T. E. Drake, T. C. Briles, and S. B. Papp, "Tantala kerr nonlinear integrated photonics," *Optica*, vol. 8, no. 6, pp. 811–817, Jun. 2021. [Online]. Available: https://opg.optica.org/optica/abstract.cfm?URI=optica-8-6-811

[3] A. E. Dorche, N. Nader, E. J. Stanton, S. W. Nam, and R. P. Mirin, "Heterogeneously integrated near-infrared DFB laser on tantalum pentoxide," in *Proc. Opt. Fiber Commun. Conf.*, 2023, Paper Tu3C-6. [Online]. Available: https://opg.optica.org/abstract.cfm?URI=OFC-2023-Tu3C.6

[4] C. Xiang et al., “High-performance silicon photonics using heterogeneous integration,” *IEEE J. Sel. Topics Quantum Electron.*, vol. 28, no. 3, May/Jun. 2022, Art. no. 8200515.

[5] D. Liang, G. Roelkens, R. Baets, and J. E. Bowers, “Hybrid integrated platforms for silicon photonics,” *Materials*, vol. 3, no. 3, pp. 1782–1802, 2010. [Online]. Available: https://www.mdpi.com/1996-1944/3/3/1782

[6] Q. Yu et al., “Heterogeneous photodiodes on silicon nitride waveguides,” *Opt. Exp.*, vol. 28, no. 10, pp. 14824–14830, May 2020. [Online]. Available: https://opg.optica.org/oe/abstract.cfm?URI=oe-28-10-14824

[7] X. Guo et al., “High-performance modified uni-traveling carrier photodiode integrated on a thin-film lithium niobate platform,” *Photon. Res.*, vol. 10, no. 6, pp. 1338–1343, Jun. 2022. [Online]. Available: https://opg.optica.org/prj/abstract.cfm?URI=prj-10-6-1338

[8] F. Yu et al., “High-power high-speed MUTC waveguide photodiodes integrated on Si3N4/Si platform using micro-transfer printing,” *IEEE J. Sel. Topics Quantum Electron.*, vol. 29, no. 3, May/Jun. 2023, Art. no. 3800106.

[9] A. Y. Liu and J. Bowers, “Photonic integration with epitaxial III–V on silicon,” *IEEE J. Sel. Topics Quantum Electron.*, vol. 24, no. 6, Nov./Dec. 2018, Art. no. 6000412.

[10] Y. Geng, S. Feng, A. W. O. Poon, and K. M. Lau, “High-speed InGaAs photodetectors by selective-area MOCVD toward optoelectronic integrated circuits,” *IEEE J. Sel. Topics Quantum Electron.*, vol. 20, no. 6, Nov./Dec. 2014, Art. no. 3801807.

[11] S. Yanikgonul et al., “Integrated avalanche photodetectors for visible light,” *Nature Commun.*, vol. 12, no. 1, Mar. 2021, Art. no. 1834. [Online]. Available: http://dx.doi.org/10.1038/s41467-021-22046-x

[12] S. Cuyvers et al., “Heterogeneous integration of Si photodiodes on silicon nitride for near-visible light detection,” *Opt. Lett.*, vol. 47, no. 4, pp. 937–940, Feb. 2022. [Online]. Available: https://opg.optica.org/ol/abstract.cfm?URI=ol-47-4-937

[13] E. Ozbay, K. Li, and D. Bloom, “2.0 ps, 150 GHz GaAs monolithic photodiode and all-electronic sampler,” *IEEE Photon. Technol. Lett.*, vol. 3, no. 6, pp. 570–572, Jun. 1991.

[14] Z. Xie, Z. Zhou, L. Li, Z. Deng, H. Ji, and B. Chen, “High-speed 850nm photodetector for zero-bias operation,” *IEEE J. Sel. Topics Quantum Electron.*, vol. 28, no. 2, Mar./Apr. 2022, Art. no. 3801007.

[15] M. S. Ünlü et al., “High bandwidth-efficiency resonant cavity enhanced Schottky photodiodes for 800–850nm wavelength operation,” *Appl. Phys. Lett.*, vol. 72, no. 21, pp. 2727–2729, May 1998. [Online]. Available: https://doi.org/10.1063/1.121073

[16] M. Jafari, T. Fatema, D. R. Carlson, S. B. Papp, and A. Beling, “Heterogeneous integration of AlGaAs/GaAs photodiodes on tantala waveguides for visible-light applications,” in *Proc. Conf. Lasers Electro-Op.*, 2022, Paper STu5G.5. [Online]. Available: https://opg.optica.org/abstract.cfm?URI=CLEO_SI-2022-STu5G.5

[17] R. Zhou et al., “Thermal stability of SU-8 low-loss optical coupling interconnects at 850 nm,” *IEEE Photon. Technol. Lett.*, vol. 36, no. 3, pp. 159–162, Feb. 2024.

[18] J. Goyvaerts et al., “Transfer-print integration of GaAs p-i-n photodiodes onto silicon nitride waveguides for near-infrared applications,” *Opt. Exp.*, vol. 28, no. 14, pp. 21275–21285, Jul. 2020. [Online]. Available: https://opg.optica.org/oe/abstract.cfm?URI=oe-28-14-21275

[19] Y. Wan et al., “Monolithically integrated InAs/InGaAs quantum dot photodetectors on silicon substrates,” *Opt. Exp.*, vol. 25, no. 22, pp. 27715–27723, Oct. 2017. [Online]. Available: https://opg.optica.org/oe/abstract.cfm?URI=oe-25-22-27715

[20] D. E. Aspnes, S. M. Kelso, R. A. Logan, and R. Bhat, “Optical properties of $\mathrm{Al}_x\mathrm{Ga}_{1-x}\mathrm{As}$,” *J. Appl. Phys.*, vol. 60, no. 2, pp. 754–767, 1986. [Online]. Available: https://api.semanticscholar.org/CorpusID:94883627

[21] P. Houston and A. Evans, “Electron drift velocity in n-GaAs at high electric fields,” *Solid-State Electron.*, vol. 20, no. 3, pp. 197–204, 1977. [Online]. Available: https://www.sciencedirect.com/science/article/pii/0038110177901848

[22] P. Gundlapalli et al., “Visible-light integrated PIN avalanche photodetectors with high responsivity and bandwidth,” *J. Lightw. Technol.*, vol. 41, no. 8, pp. 2443–2450, Apr. 2023.

[23] Y. Lin. et al., “Monolithically integrated, broadband, high-efficiency silicon nitride-on-silicon waveguide photodetectors in a visible-light integrated photonics platform,” *Nature Commun.*, vol. 13, no. 1, Oct. 2022, Art. no. 6362. [Online]. Available: https://doi.org/10.1038/s41467-022-34100-3